



Novel nano-biosorbent materials from thermal catalytic degradation of green pea waste for cationic and anionic dye decolorization

Norbert Onen Rubangakene¹ · Marwa Elkady^{2,3} · Ahmed Elwardany^{4,5} · Manabu Fujii⁶ · H. Sekiguchi⁷ · Hassan Shokry^{1,8}

Received: 25 June 2022 / Revised: 28 August 2022 / Accepted: 11 September 2022 / Published online: 27 September 2022
© The Author(s) 2022

Abstract

The recycling of waste materials in wastewater decontamination has been an attractive discipline in zero discharge and energy recovery. Biochar/zeolite nanocomposite has been successfully synthesized as a cheap and eco-friendly material from a solid fraction obtained from the thermo-catalytic conversion of green pea agriculture waste (*Pisum sativum*). A dark-whitish solid was obtained from thermal pyrolysis at 450 °C with a heating rate of 27 °C/min for 15 min that was further subjected to alkaline chemical activation. The synthesized composites have been examined using Fourier transform infrared spectroscopy (FTIR), scanning electron microscopy (SEM), energy dispersive X-ray (EDX), X-ray diffraction (XRD), transmission emission microscopy (TEM), and Brunauer-Emmet-Teller (BET) analyses. The successful preparation of biochar/zeolite nanocomposite was evident from characterization results with an average particle size of 30–40 nm with a high surface area of 15.3 m²/g. The material was evaluated as an eco-friendly adsorbent for decolorization of both cationic methylene blue dye (MB) and Congo red anionic dye (CR) using the batch technique. The influence of dosage, pH, temperature, initial dye concentration, and contact time were studied against the dye adsorption process. It was indicated that the material recorded maximum dye decolorization efficiencies of 87.5% at pH of 12 and 84.1% at pH of 2 for MB and CR, respectively. The optimum material dosage and contact time for dye decolorization were 5 g/l and 60 min, respectively. Thermodynamic parameters were calculated from the sorption process and revealed a negative charge of Gibbs free energy (ΔG°) an indication of spontaneity and thermodynamic favorability. Positive enthalpy and entropy demonstrated the endothermic behavior and the disorderliness. Equilibrium adsorption results best fitted to the Langmuir isotherm model, while MB and CR adsorption kinetics were pseudo-second-order reactions.

Keywords Composite · Thermo-catalytic conversion · *Pisum sativum* · Langmuir isotherm · Dye removal

✉ Norbert Onen Rubangakene
norbert.rubangakene@ejust.edu.eg

✉ Hassan Shokry
hassan.shokry@ejust.edu.eg

¹ Environmental Engineering Department, Egypt-Japan University of Science and Technology (E-JUST), New Borg El-Arab City 21934, Alexandria, Egypt

² Chemical and Petrochemical Engineering Department, Egypt-Japan University of Science and Technology (E-JUST), New Borg El-Arab City 21934, Alexandria, Egypt

³ Fabrication Technologies Researches Department, Advanced Technology and New Materials Research Institute, City of Scientific Research and Technological Applications (SRTA-City), Alexandria, Egypt

⁴ Energy Resources Engineering Department, Egypt-Japan University of Science and Technology (E-JUST), New Borg El-Arab 21934, Egypt

⁵ Faculty of Engineering, Mechanical Engineering Department, Alexandria University, Alexandria 21544, Egypt

⁶ Department of Civil and Environmental Engineering, Tokyo Institute of Technology, Meguro-ku, Tokyo 152-8552, Japan

⁷ Chemical Science and Engineering Department, Tokyo Institute of Technology, S-4, 2-12-1 Ookayama, Meguro-ku, Tokyo 152-8552, Japan

⁸ Electronic Materials Researches Department, Advanced Technology and New Materials Research Institute, City of Scientific Research and Technological Applications (SRTA-City), Alexandria, Egypt

1 Introduction

Population and industrial growth increased the utilization of dyes by the population to meet sustainable national development in industries such as leather, textile, cosmetics, paper, and printing using acidic, basic, reactive, direct, and dispersive dyes [1, 2]. Dyes constitute two major organic compounds of chromophores and auxochromes which are responsible for color and intensities, respectively [3]. These organic structures are complex, non-biodegradable, carcinogenic, and teratogenic and have toxicity effects on the environment [4, 5]. Without treatment, dye-loaded wastewater disrupts natural water's chemical properties, and adversely impacts aesthetics, resulting in the death of aquatic flora and fauna and health hazards to humans within the vicinity of this polluted discharge [6]. Numerous physical, chemical, and biological techniques such as oxidation, photocatalysis, phytoextraction, reverse osmosis, electrolysis, membrane treatment, and coagulation have been invented to remediate dye contaminants in wastewater [7–9]. However, these methods have associated drawbacks of less performance effectiveness, time-consuming, and involvement of high operational and maintenance costs [10, 11].

Recent studies have presented adsorption and mass transfer operations as the most attractive alternative for pollutant separation due to economical scalability, effectiveness, environmental benignity, ease of applications, and abundance of adsorbents [12]. Moreover, prominently used adsorbents such as activated carbon possess high surface area, porous morphology, and surface chemistry to remove dyes from wastewater [13]. Nevertheless, activated carbons are expensive and difficult to regenerate [14]. Thus, cheap alternative materials such as zeolite, graphene oxides, and natural wastes such as mango seed kernel, pineapple leaf powder, wheat bran, eggshell, and groundnut shell have been exploited [1, 10–15]. These materials are utilized directly or after light physicochemical treatment, such as carbonization. However, these biomass-derived materials have hydrophobic functional groups that make them less sensitive and dispersive in aqueous media, causing low adsorption capacity, low adsorbate-adsorbent interaction, and difficulty in regenerations [12].

Biomass, biodegradable organic materials from plants and animals, has been instrumental in sustainable development through renewable energy resources, carbon sequestration, and the production of biomaterials [16]. Biomass conversion exploits physical extractions, thermochemical, and biochemical conversions into high energy materials for electricity, heat, and fuel [1]. Pyrolysis is the most attractive technique using anoxic conditions to thermally degrade carbon-neutral materials producing enriched

energy products such as biochar, bio-oil, and syngas which are valuable in environmental applications [17]. Catalysis exploits the increment of the biomass carbonization process by adding reagents such as metal oxides, zeolites, and silica-alumina to reduce operational conditions and attain high yielded pyrolysis products [18]. This process is achieved through an in situ catalytic pyrolysis process, where biomass and catalyst are mixed, or an ex situ catalytic pyrolysis process, where pyrolysis vapor passes over the catalyst. Zeolite has been the most efficient catalyst because of its acidity and shape selectivity. It is beneficial for producing aromatic compounds at temperatures as low as 550 °C compared to other catalysts such as metals and metal oxides [19]. Moreover, it can produce multiple products of bio-oil, syngas, and solid fraction. The liquid and gaseous products have been a great interest in energy technology. On the other hand, the solid fraction possesses residual enhanced functional groups with great potential for green sorbent in the ever-growing and demanding mass transfer wastewater treatment systems.

This study aims to propose an innovative method of producing a valuable solid fraction of biochar/zeolite nanocomposite from in situ catalytic pyrolysis of green pea peels onto zeolite catalyst followed by alkaline activation. So, the agricultural waste will be converted into novel advanced and eco-friendly valuable nanocomposite material. This nanocomposite was evaluated as a novel adsorbent and its effectiveness in decolorization of two different dye types from aqueous solutions. The authors deduced that synthesized material will exhibit abundant functional groups and sorption sites beneficial for wastewater purification. The structural and textural properties of the synthesized material were characterized by EDX, SEM, TEM, FTIR, XRD, and BET. A detailed study was performed on the effects of dye treatment parameters such as temperature, pH, dosage, initial concentration, and contact time. In an attempt to identify the dye decolorization process mechanism, adsorption isotherm, kinetics, and thermodynamics of the adsorption process were evaluated.

2 Materials and methods

2.1 Materials and reagents

Green pea peels (GPP) were collected from Alexandria local market. Zeolite analytical reagent was procured from the Central Drug Housing, India. Sodium chloride (99%) was from the Alpha Chemical, India. Sodium hydroxide (97%) was purchased from the Alpha Chemical, Egypt. Potassium hydroxide (86%) was derived from the Dop Organik, Turkey. Hydrochloric acid (37% HCl) was procured from the Piochem,

Egypt. Nitric acid (67%) was supplied from the KGea, Merck, Germany. Ammonium chloride (99%) was supplied from the Acros Organic, Belgium. Methylene blue was obtained from the Alpha Chemical, Egypt, with chemical formula $C_{16}H_{18}N_3SCI$, $Mw = 319.85 \text{ g. mol}^{-1}$ (99%). Congo red with the chemical formula $C_{32}H_{22}N_6Na_2O_6S_2$, $Mw = 327.34 \text{ g. mol}^{-1}$ (99%), was an analytic reagent purchased from the Central Drug Housing, India.

2.2 Methods

2.2.1 Preparation of green pea peels (GPPs)

The GPPs wastes were washed with distilled water several times to eliminate dirt and contaminants. It was dried under sunlight for 48 h, and later in a dryer at $105 \text{ }^\circ\text{C}$ for 48 h. Dried GPPs wastes were crushed using an electric blender to obtain sizes less than 1 mm, after which they were ball milled to sizes less than $212 \text{ }\mu\text{m}$.

2.2.2 Activation of zeolite catalyst

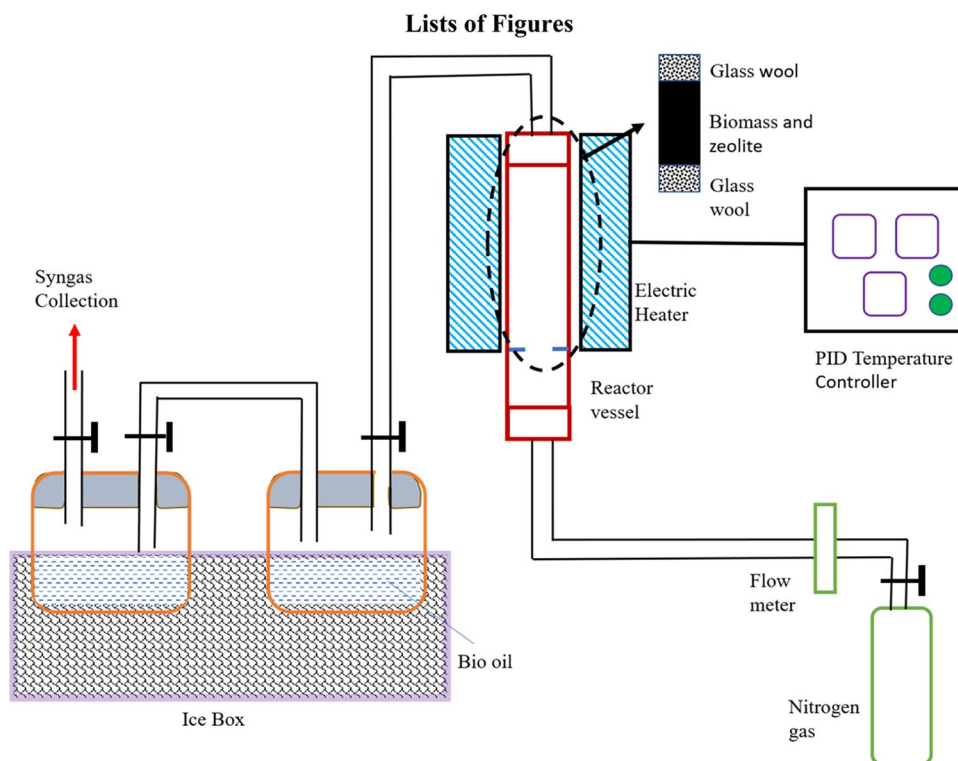
Zeolite was protonated using the method by Ren et al. [20]. Ten grams of zeolite was activated at 400 mL of 0.3 M NaOH solution and stirred for 2 h at $85 \text{ }^\circ\text{C}$. The hierarchical porous zeolite material was dried in an oven at $105 \text{ }^\circ\text{C}$, and

the material was cooled and kept in the desiccator for further utilization as activated catalytic material.

2.2.3 Catalytic pyrolysis of GPP for production of biochar/zeolite bio-composite nanomaterial

The in situ catalytic pyrolysis system consisted of a fixed bed system, electric furnace, and stainless-steel tubular reactor with dimensions equal to 30 cm in length and 5 cm in diameter with a total of 150 ml volume. This reactor was loaded with substrates kept inert under a supply of nitrogen. A thermocouple is attached to the heating medium to observe the temperature. At the start of the pyrolysis process, nitrogen at 20 ml/min is purged into the reactor system for 5 min to limit any due oxidation process. GPP waste and activated zeolite in a mixing ratio of 10:1 were placed at the reactor and heated at $450 \text{ }^\circ\text{C}$ at a ramping rate of $27 \text{ }^\circ\text{C}/\text{min}$ for 15 min, as shown in Fig. 1. The pyrolysis residue (solid fraction) was weighed, and its yield was determined [21]. The yielded solid fractions from the catalytic pyrolysis process were further activated using 1 M of NaOH solution. The alkali activation process was performed through the solid fraction treatment with NaOH in a mixing ratio (1.0 g/20 ml W/V ratio) under heating at $450 \text{ }^\circ\text{C}$ for 1 h [22]. The prepared adsorbent material was designated as an activated biochar/zeolite composite (ABZC) nanomaterial.

Fig. 1 Thermal catalytic set-up of the process



2.2.4 Characterization of prepared bio-composite nanomaterial

The physico-chemical properties of the prepared activated biochar/zeolite composite (ABZC) nanomaterials were evaluated. The functional groups incorporated at the prepared ABZC were determined by FTIR (Shimadzu 8400 s, Japan) in a spectra range of 400–4000 cm^{-1} using KBr pellet as a matrix containing 0.1% composite material. The morphological changes in prepared material were determined using SEM (JEOL, JSM-6010LV, Japan). The quantitative elemental compositions and high-resolution images were determined by EDX equipped with TEM imaging (JEOL, JEM-2100F, Japan). The material crystallinity was analyzed using the Bruker 2D phase XRD method in the angle range of 10–80° exploiting Cu- α radiation. Nitrogen adsorption and desorption analyses were performed to determine pore properties using Microtrac MRB Belsorp Mini X, Japan. The sample was subjected to overnight degassing at 180 °C before analysis.

2.2.5 Point of zero charge

The PH_{PZC} of the prepared ABZC nanocomposite was determined by methods by K. Mensah et al. [23]. One hundred fifty milligrams of adsorbent was added to 100 ml of 0.1 M NaCl solution. The pH of the solution was adjusted between 2 and 12 using 0.1 M HNO_3 and 0.1 M KOH. The solutions were shaken by an orbital shaker at 170 rpm for 24 h at room temperature to achieve equilibration. The change in solution pH was measured and plotted against the initial pH.

2.2.6 Preparation and analysis of adsorbate solutions

Two different industrial dye types of cationic MB and anionic CR were selected as model water pollutants due to their draconian environmental and human effects. Stock solutions with 500 mg/l initial concentrations were prepared from each dye type by dissolving 0.5 g of the dye in 1 l of doubly distilled water and stirred until complete homogeneity. Subsequent dilutions from each stock solution have lower concentrations of the dye solutions.

The remaining dye solution concentrations after the treatment process were determined using a UV–Vis spectrophotometer (JASCO 360 spectrophotometer, Japan) from a standard calibration curve prepared by measuring the absorbance of known dye concentrations at maximum wavelengths of 663 nm and 504 nm for MB and CR, respectively. The pH of the solution was determined using a multiparameter reader (JENWAY 370 pH meter, UK).

2.3 Evaluation of the adsorption performance of ABZC nanocomposite toward anionic and cationic dyes

The prepared ABZC nanocomposite was tested as a bio-adsorbent to remove cationic MB and anionic CR dyes from synthetic wastewater solutions using a batch adsorption technique using a batch adsorption technique at 250 mL capped volumetric flask agitated at 170 rpm by Orbital shaker (INCU Mini shaker, USA). Parameters such as adsorption dosage (50–250 mg), initial dye concentration (50–250 mg/l), solution pH (2–12), solution temperature (20–50 °C), and contact time (0–90 min) were studied. The pH of the solution was adjusted using 0.1 M NaOH and 0.1 M HCl. Final concentrations of the treated solutions were determined for supernatant liquid after centrifugation at 6000 rpm for 7 min. The final concentrations were calculated from a pre-determined calibration curve. Percentage removal and uptake capacity (q_t) of the prepared ABZC nanocomposite were calculated from the following Eqs. 1 and 2 [24].

$$\% \text{ removal} = \frac{C_0 - C_t}{C_0} * 100\% \quad (1)$$

$$q_t = \frac{C_0 - C_t}{W} * V \quad (2)$$

where q_t is the dye uptake capacity (mg/g) at a time, t ; C_0 is the initial dye concentration; C_t is the dye concentration at time t ; W is the dry weight of adsorbent used; and V is the volume of solution.

After dye removal, the resulting solid materials that adsorbed dyes were filtered, dried in an oven, and characterized by FTIR and SEM as an attempt to investigate the adsorption mechanism.

3 Results and discussions

3.1 Influence of adsorption processing parameters

3.1.1 Influence of contact time

The contact time of the adsorption process is a paramount factor that directly influences the kinetics of the reactions. Figure 2 revealed the influence of contact time on both the CR and MB dye removal onto the prepared ABZC nanocomposite at a constant dosage of 5 g/l with 50 mg/l initial dye concentration, pH 7, and temperature at 25 °C. In both cases, the dye removal process was rapid at the initial stages, attaining 73.64% for MB and 31.6% for CR within the first 10 min. This high increment can be explained by the

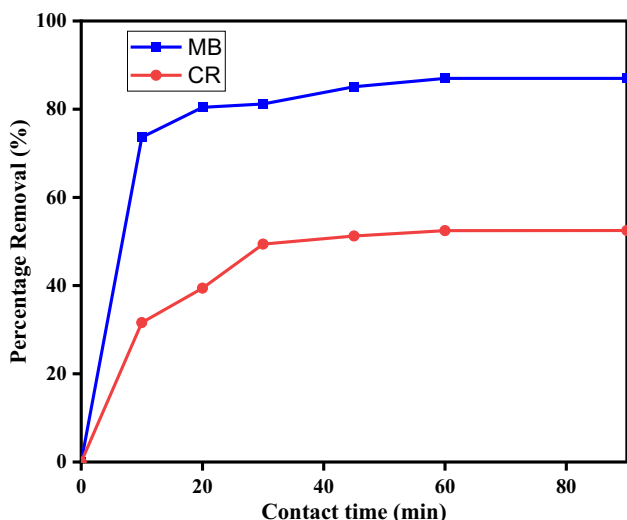


Fig. 2 Effect of contact time on percentage removal of MB and CR

accessibility of sizeable active adsorbent sites to be interacted with the dye molecules [20]. The equilibrium state was recorded at 20 and 30 min for MB and CR, respectively. After equilibrium, there was a slight increment in dye percentage removal with time. This phenomenon is attributed to the saturation of ABZC active sites [25]. Considerately, the MB and CR sorption equilibration time was fixed at 60 min to ensure the completion of the adsorption process.

3.1.2 Influence of adsorbent dosage

The influence of ABZC nanocomposite dosages (5–25 g/l) on dye percentage removal was performed at constant initial dye concentrations of 50 mg/l, pH 7 at contact time of 60 min, and solution temperature of 25 °C. Figure 3 revealed the improvement of dye percentage removal from 83.9 to 86.9% for MB and from 46.1 to 53.3% for CR with increasing material dosages from 5 to 25 g/l. Contrarily, the uptake capacity decreases from 83.9 to 17.4 mg/g for MB and from 46.1 to 10.7 mg/g for CR dye with increasing material dosages from 5 to 25 g/l. [26]. A rapid increase in percentage MB removal to 83.9% and 46.1% for CR dye at a dosage of 25 mg/l is attributed to the increment in material surface area and active sites available for the adsorption process [27]. Reduction in MB and CR dye uptake capacity is attributed to more active sites available against few dye molecules to occupy the active sites leaving most active sites unoccupied [28].

3.1.3 Influence of initial dye concentration

The influence of initial dye concentrations ranged from 50 to 250 mg/l was studied at a constant material dosage

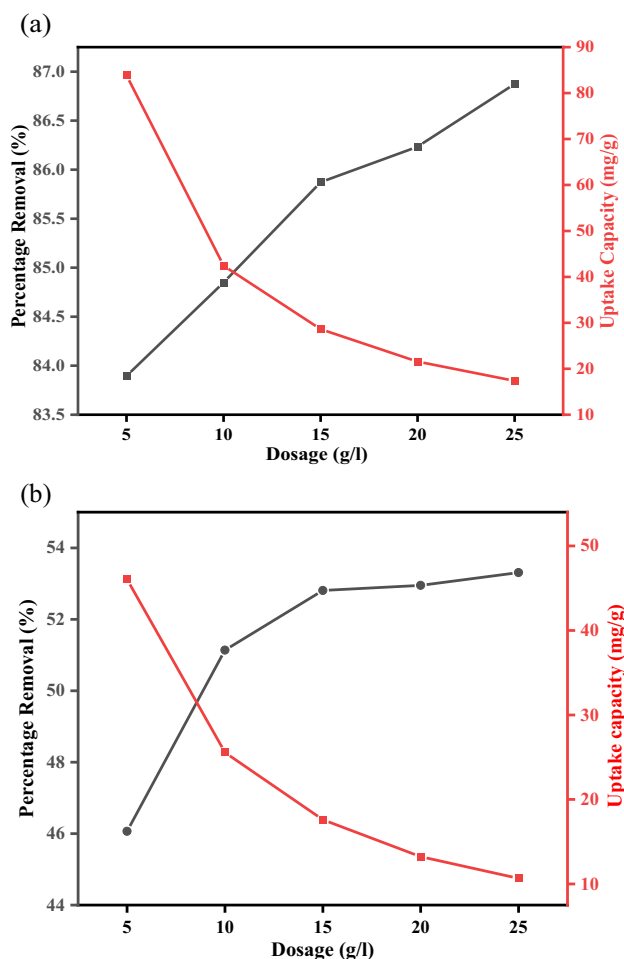


Fig. 3 Effect of adsorbent dosage on percentage removal and uptake capacity of a MB and b CR

of 5 g/l at neutral solution pH and room temperature for 60 min. Figure 4 revealed enhanced dye uptake capacity with an increment in the initial concentration for both CR and MB. Popularly, the adsorption process depends mainly on the concentration gradient, presence of adsorbent active sites, adequate amounts of MB and CR molecules, porosity, and surface area of adsorbent beside the available functional groups for electrostatic attraction of pollutants [29]. Consequently, there is a rise in dye uptake capacity from 83.2 to 387.9 mg/g for MB and from 51.4 to 144.9 mg/g for CR dye with increasing initial dye concentration from 50 to 250 mg/l. The increment is attributed to the driving force for mass transfers that originated from concentration gradient and the ability of more dye molecules to surround active sites of the ABZC nanocomposite material at fixed dosages [30, 31].

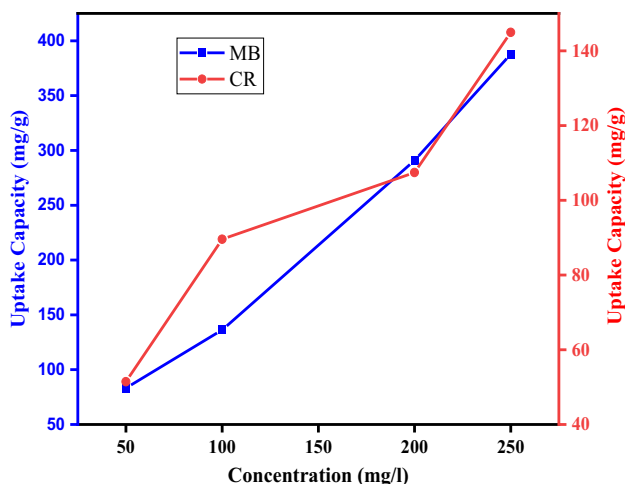


Fig. 4 Illustration of effect of initial concentration on uptake capacity of MB and CR

3.1.4 Influence of solution temperature

Temperatures' contribution to the adsorption process is instrumental in understanding the thermodynamics of the adsorption process. Figure 5 revealed the influence of solution temperature from 20 to 50 °C in presence of a constant ABZC dosage of 5 g/l for 60 min and neutral pH. There was a substantial enhancement of MB and CR dye removal from

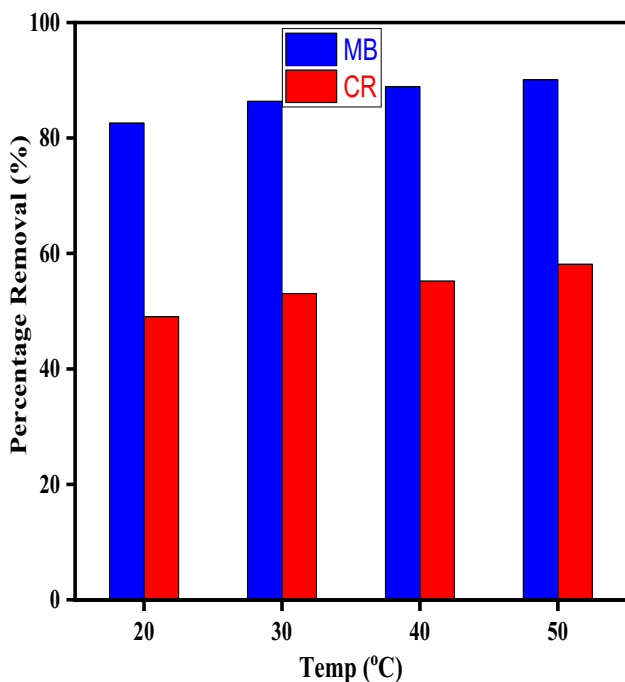


Fig. 5 Influence of temperature on removal of MB and CR

82.6 to 90.1% and from 49.0 to 58.1%, respectively. This phenomenon may be elucidated by the increment in temperature speeds up the mobility of the MB and CR dye molecules granting numerous dye molecules to obtain sufficient energy to interact with the ABZC active sites. Furthermore, the increase in solution temperature may increase the internal swelling in the adsorbent's pore structures that allows more dye molecules to penetrate the ABZC material [32]. Accordingly, the adsorption of MB and CR onto synthesized ABZC nanocomposite can be predicted as endothermic.

3.1.5 Influence of solution pH

pH performs an instrumental role in regulating the charges on the ABZC surface and the ionization degree of CR and MB dye molecules during the adsorption process. Figure 6 revealed the effect of solution pH at the studied range of 2–12 using a constant 5 g/l from ABZC dosage. The adsorbent's point of zero charge (PH_{PZC}) is also determined as an isoelectric point (IEP) which describes the point at which the surface of the adsorbent is neither basic nor acidic. PH_{PZC} of the composite was estimated as 7.3 from a plot of ΔpH versus pH (Fig. 7). At $\text{pH} < \text{PH}_{\text{PZC}}$, the surface of the ABZC is positively charged, while at $\text{pH} > \text{PH}_{\text{PZC}}$, the surface of the ABZC is negatively charged [33]. The behavior is associated with protonation and deprotonation, respectively.

It was indicated from Fig. 6 that MB dye removal was enhanced from 29.3 to 87.5% with increasing solution pH from 2 to 12. On the other hand, CR dye removal was amplified from 29.7 to 84.1% by increasing the solution acidity [20]. At the basic solution, the adsorbent

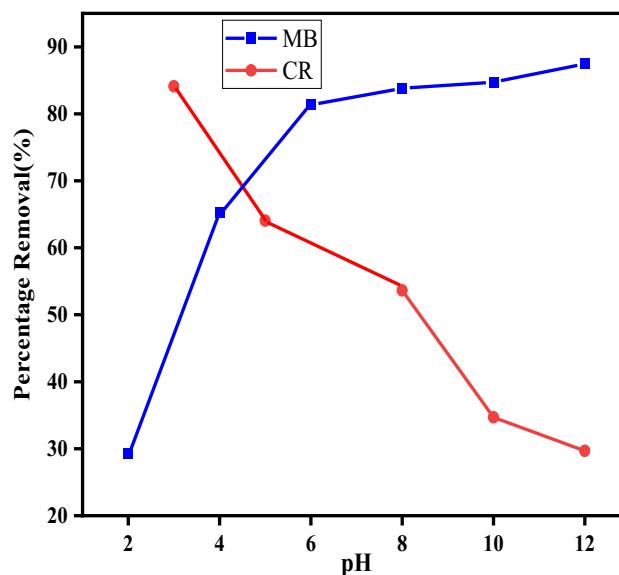


Fig. 6 Effect of solutions pH on the percentage removal of MB and CR

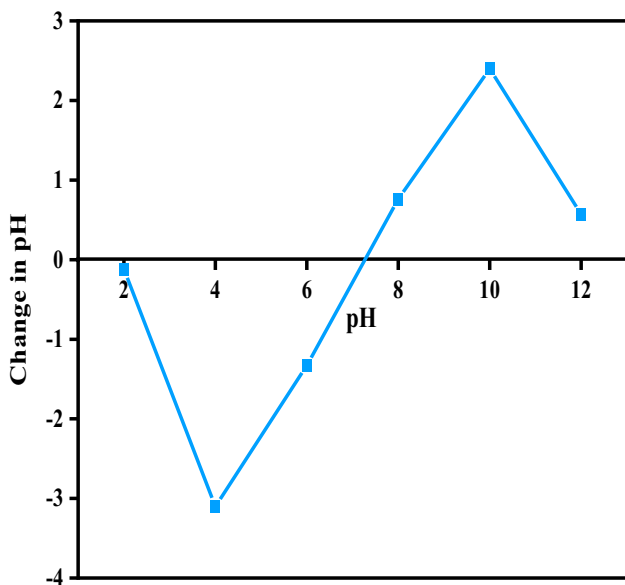


Fig. 7 Study of point of zero charge of the adsorbent

surface acquires negative charges due to deprotonation. Thus repulsion force is predominant between the anionic CR dye molecules and the negatively charged adsorbent surface leading to lower dye removal [34]. Contrarily, an attraction is shared between the negatively charged adsorbent and the cationic MB molecules increasing the dye removal. Similarly, in an acidic solution, positive charges are acquired onto the adsorbent surface due to protonation. Accordingly, electrostatic repulsion occurs between the positively charged adsorbent surface and cationic MB dye molecules, whereas attractive forces occur between the anionic CR dye molecules and the positively charged adsorbent [35]. Moreover, the decrease in MB dye removal at a solution of pH = 2 is may be ascribed to the dissolution of aluminum ions in the zeolite matrix that may take place at high solution acidity [36].

3.2 Adsorption equilibrium

Adsorption equilibrium isotherms represent the distribution of MB and CR dye molecules on both solid and liquid phases. Therefore, models offer insight into the affinities and surface properties of the adsorbents [37]. The interactions between MB and CR dye molecules on the ABZC surface with the dye molecules in solutions can be comprehensively investigated using adsorption isotherms. Commonly applied adsorption isotherms in comprehension of the nature of adsorption are described as the following.

3.2.1 Langmuir model

Langmuir’s model describes the adsorption process on the homogeneous monolayer surface of the adsorbent. This model utilizes significant assumptions of adsorption sites being equally probable, and the active sites do not undergo interactions with one another until fully occupied the surface. Langmuir model is expressed as Eq. 3 [38].

$$q = \frac{q_{max}K_{lc}}{1 + K_{lc}} \tag{3}$$

The expression of the linearized Langmuir model is presented in Eq. 4 [39]:

$$\frac{1}{q_e} = \frac{1}{K_l q_m} \frac{1}{C_e} + \frac{1}{q_{max}} \tag{4}$$

where q_e (mg/g) refers to the quantity of CR and MB adsorbed at equilibrium, C_e (mg/l) is equilibrium concentration, and k_L (L/mg) and q_{max} (mg/g) are Langmuir constants relating to energy of adsorption. Graphical representations of $1/C_e$ versus $1/q_e$ (Fig. S2a i & ii) were straight lines. Langmuir constants were obtained from the slopes and intercepts of the graphs, and the results are presented in Table 1.

It was evident from Table 1 that R^2 values were calculated as 0.9346 and 0.9779 for MB and CR dyes, respectively, exhibiting good linearity and strong evidence of the applicability of Langmuir isotherm for describing the sorption process of the studied dye types onto the prepared adsorbent. This assumes uniform sorbent distribution and monolayer coverage of dye molecules onto the ABZC nanocomposite surface. The q_{max} value for MB adsorption was recorded as

Table 1 Adsorption isotherm of the composite after interaction with MB and CR

Isotherm parameter (type of model)	Parameters	Values	
		MB	CR
Langmuir	q_{max} (mg/g)	534.8	163.9
	R_L	0.4853	0.5123
	K_L (L/mg)	0.0212	0.0190
	R^2	0.9346	0.9779
Freundlich	K_f	14.09	14.36
	$1/n$	0.7882	0.4218
	R^2	0.9018	0.9424
Temkin	K_T (L/mg)	0.1586	0.1673
	B_T (J/mol)	161.64	37.63
	R^2	0.7213	0.941
D-R	B_D (mol ² /kJ ²)	0.00002	0.00009
	qm (mg/g)	297.97	122.8
	E (kJ/mol)	158.11	44.51
	R^2	0.6826	0.9113

534.76 mg/g which was higher than that of CR dye adsorption recorded as 163.9 mg/g. Similarly, the R_L values were 0.4853 for MB dye and 0.5123 for CR dye; all these values are within the range of 0–1 thus describing the favorability of the adsorption process.

3.2.2 Freundlich model

The Freundlich model depicts heterogeneous multilayer adsorption systems of MB and CR dyes adsorption, considering an assumption of different active sites with varying adsorption energies. Freundlich's model is expressed as Eq. 5 [39]:

$$q_e = k_f C_e^{\frac{1}{n}} \quad (5)$$

The linearized expression of the model is investigated in Eq. 6:

$$\log q_e = \frac{1}{n} \log C_e + \log k_f \quad (6)$$

where k_f is the Freundlich constant relating to uptake capacity, whereas n is a constant depicting adsorption intensity, both attainable from the graph. The plots of $\log q_e$ against $\log C_e$ (Fig. S2b i & ii) are straight lines. The estimated parameters are presented in Table 1.

The results revealed that the magnitude of parameter $1/n$ was 0.7882 and 0.4218 for MB and CR dyes, respectively, which are lower than 1. These results describe the favorable adsorption process of the dye molecules onto the ABZC surface. It was also evident that R^2 values of 0.9018 for MB and 0.9428 and CR dye adsorption were lower than the corresponding Langmuir values indicating that these adsorption processes do not closely adhere to the Freundlich model.

3.2.3 Temkin model

The Temkin model accounts for the heterogeneous surface of the adsorbent while manifesting adsorbate-adsorbent interactions. The model also relies on the following assumptions: (i) heat of adsorption of CR and MB molecules in the layer diminishes linearly with coverage owing to dyes-composites interactions and (ii) a distinct adsorption characteristic is the stable distribution of binding energies to the maximum binding energy. Temkin model is expressed as Eq. 7:

$$q_e = \frac{RT}{b} \ln(K_T C_e) \quad (7)$$

The linear form of the model is linearized in Eq. 8:

$$q_e = B \ln K_T + B \ln C_e \quad (8)$$

where $B = \frac{RT}{b}$ is the Temkin constant relating to the heat of adsorption, whereas K_T is the equilibrium constant

responding to the binding energy. Representations of plots of q_e versus $\ln C_e$ (Fig. S2c i & ii) are straight lines with other constants presented in Table 1.

The values of R^2 were calculated as 0.7213 and 0.941 for MB and CR dyes, respectively. These values are less than those calculated by Langmuir and Freundlich, indicating that the Temkin model does not closely describe these adsorption processes. The binding constant value of K_T was calculated as 0.1673 for CR which was greater than that of MB that equals to 0.1586. These results confirm the stronger binding of CR dye to the ABZC surface compared with MB dyes molecules.

3.2.4 Dubinin–Radushkevich model

D-R model describes the adsorption phenomenon based on pore structure on the ABZC surface. The B_D constant relates to the mean free energy per mole of dye transferred from the intrinsic distribution in solution to the solid phase. D-R model best established whether the mechanism of the adsorption process is physical or chemical and is described by Eq. 9 [40]:

$$q_e = q_o \exp \left(-B_D \left[RT \ln \left(1 + \frac{1}{C_e} \right)^2 \right] \right) \quad (9)$$

The linear illustration of the D-R isotherm is linearized in Eq. 10:

$$\ln q_e = \ln q_o - B_D \mathcal{E}^2 \quad (10)$$

where q_D is the D-R constant which reflects the degree of sorbate adsorption by the ABZC surface, and B_D is a constant relating to the mean free energy of adsorption. \mathcal{E} is a Polanyi potential described by the equation $\mathcal{E} = RT \ln \left(1 + \frac{1}{C_e} \right)$;

The linearized plots of \mathcal{E}^2 versus $\ln q_e$ (Fig. S2d i & ii) yielded a correlation coefficient R^2 of 0.6826 and 0.9113 for

Table 2 Kinetics parameters after MB and CR removal

Kinetic parameter (type of model)	Parameters	Values	
		MB	CR
Pseudo-first order	K_1 (min^{-1})	−0.0021	−0.00103
	q_e , exp (mg/g)	83.17	51.44
	q_e , cal (mg/g)	52.54	73.27
	R^2	0.9024	0.963
Pseudo-second order	K_2 (mg/g/min)	0.0085	0.0042
	q_e , exp (mg/g)	83.17	51.44
	q_e , cal (mg/g)	87.72	55.25
	R^2	0.9983	0.9923
Intraparticle diffusion	C	18.73	13.16
	K_{id}	10.70	4.788
	R^2	0.7792	0.7628

MB and CR dyes, respectively. Other calculated constants are presented in Table 2.

It was evident that the magnitude of the calculated correlation coefficient was lower than those obtained from other models indicating that D-R was the least fit for these sorption processes. Additionally, the values of free energy, E , were 158.1 kJ/mol for MB and 44.51 kJ/mol for CR dye, which were higher than 8 kJ/mol, indicating that the sorption was a chemical process [40].

3.3 Kinetic models

The rates at which MB and CR dyes were adsorbed on sorbent surfaces are paramount for evaluating reaction kinetics using a theoretical model for associated benefits of design and control of adsorption units [41]. Possible pseudo-first-order, pseudo-second-order, and intraparticle diffusion applications were tested, and linear regression coefficient R^2 was used to select the best fit model for evaluating the nature of the adsorption process.

3.3.1 Pseudo-first-order

The first-order model exploits the CR and MB dye uptake changes with time, relating to the difference between saturation dye concentrations and the amount of dyes adsorbed with time.

Pseudo-first-order was evaluated from a linear expression according to Eq. 11 [42]:

$$\ln(q_e - q_t) = \ln q_e - k_1 t \quad (11)$$

where q_e and q_t (mg/g) are amounts of CR and MB adsorbed at equilibrium and time, t , respectively, whereas k_1 (min^{-1}) is a first-order reaction constant. Values of q_e , k_1 and R^2 calculated from the linearized graphical representations of $\ln(q_e - q_t)$ against t (Fig. S3) that fit first-order are tabulated in Table 2.

The graphic illustrations suggested low R^2 values of 0.9024 and 0.963 for MB and CR dyes, respectively, implying that the processes were not closely related to the first order. Moreover, the values of $q_{e_{\text{exp}}}$ and $q_{e_{\text{cal}}}$ substantially deviate from each other, confirming that the dye sorption processes onto ABZC are not first order.

3.3.2 Pseudo-second-order

The second-order model exploits the assumption of chemical interactions between CR and MB dyes onto ABZC material surfaces. The expression of this model is presented in Eq. 12 [43]:

$$\frac{dq_t}{dt} = k_2 (q_e - q_t)^2 \quad (12)$$

The illustration of a linearized form of the model is illustrated in Eq. 13:

$$\frac{t}{q_t} = \frac{t}{k_2 q_e^2} + \frac{t}{q_e} \quad (13)$$

where k_2 (g/mg/min) is the second-order kinetic equilibrium constant, q_t and q_e (mg/g) are the quantities of MB and CR adsorbed at the time (t) and equilibrium, respectively. The investigation of this model was recorded from the plot of $\frac{t}{q_t}$ against t (Fig. S4), revealing straight line graphs and other calculated parameters presented in Table 2. The R^2 values were 0.9923 for CR dye and 0.9983 for MB dye, indicating closer compliance to the second kinetic order than the first order. Furthermore, the $q_{e_{\text{cal}}}$ and $q_{e_{\text{exp}}}$ in Table 2 are closely related in their values, confirming that the kinetics of the two dye removal processes were second-order models.

3.3.3 Intraparticle diffusion model

The intraparticle model assumes that the adsorption rate depends on the solid adsorbent properties such as size, functional groups, shape, surface area, porosity, and surface charge [44]. The expression of the linearized model is illustrated in Eq. 14:

$$q_t = k_{\text{id}} t^{1/2} + C \quad (14)$$

where k_{id} is the intraparticle diffusion rate constant. The linear graphical illustrations of q_t versus $t^{1/2}$ (Fig. S5) are to be rendered by an adsorption process that follows intraparticle diffusion, and the plot must pass through the origin.

From Fig. S5, there are substantial deviations from the origin, indicating that the removal of CR and MB dyes may not be returned to particular diffusion but other methods such as surface diffusion, surface adsorption, and film diffusion may contribute to the process. The non-zero values of 18.73 and 13.16 indicated an enhanced effect of boundary layers in removing both MB and CR dyes onto ABZC.

3.4 Thermodynamics

Thermodynamic parameters of the adsorption process are indicators for evaluating the practicability as they consider the energy and entropy to assess the possibility of a spontaneous process [45].

The thermodynamic parameters ($\Delta G^\circ = \text{Gibbs free energy change}$, $\Delta H^\circ = \text{Enthalpy change}$ and $\Delta S^\circ = \text{Entropy change}$) of uptake of CR and MB dyes onto the ABZC surface are influenced by the temperature at which the process is occurring:

$$\Delta G^\circ = -RT \ln K_L \quad (15)$$

$$\Delta H^\circ = -R \left(\frac{T_2 T_1}{T_2 - T_1} \right) \ln \frac{K_{L1}}{K_{L2}} \quad (16)$$

$$\Delta S^\circ = \frac{\Delta H^\circ - \Delta G^\circ}{T} \quad (17)$$

where equilibrium constant $k_L = \frac{C_{BE}}{C_{AE}}$

C_{AE} and C_{BE} are the equilibrium concentrations of CR or MB on solution and sorbent, respectively. Entropy and standard enthalpy were determined from the Van Hoff equation.

$$\ln k_L = \frac{\Delta S^\circ}{R} - \frac{\Delta H^\circ}{RT} \quad (18)$$

The energy of activation E_a was estimated based on the relationship between E_a and ΔH° reaction in solution.

$$E_a = \Delta H^\circ + RT \quad (19)$$

ΔS° and ΔH° were obtained from intercept and slope of linearized plots of $\ln K_L$ vs $\frac{1}{T}$ (Fig. S6) and the rest of the tabulated data are represented in Table 3.

The calculated ΔG° have negative values in the range of 0 to -20 kJ/mol implying that both CR and MB removal are spontaneous, thermodynamically favorable, and a physical process [46]. The values of ΔH° for both CR and MB dyes are within a range of 1 to 93 kJ/mol. The positive values of ΔH° confirm that the sorption dye processes are classified as endothermic processes [47]. Furthermore, the positive ΔS° values revealed increased randomness on dye-ABZC nanocomposite interface and good affinity of dyes towards ABZC during the adsorption process [48, 49].

As determined from Arrhenius Eq. 19, the activation energies involved for MB dye removal ranged from 19.65 to 19.89 kJ/mol, whereas CR dye removal ranged from 11.82 to 12.06 kJ/mol. The low value of E_a further proposes that the adsorption processes are governed by physisorption phenomena [50].

3.5 Characterization of the prepared ABZC nanocomposite bio-adsorbent

3.5.1 XRD analysis

The diffraction pattern analysis of the synthesized ABZC nanomaterial and the free activated zeolite catalyst was conducted between Bragg's angles of 10 – 80° (Fig. 8). It was evident from Fig. 8a that ABZC nanocomposite has a broad peak at 20 – 30° . This broad peak indicated the coexistence of carbonaceous material, while the crystalline peaks were crystal traces of zeolite. This is further validated by the diffractogram in Fig. 8b that predominated with sharp crystals of zeolite type Y or Fajausite materials (ICCD standard No 071–0987). The main constituents of zeolite crystals were quartz (SiO_2) which appears at the characteristic peaks

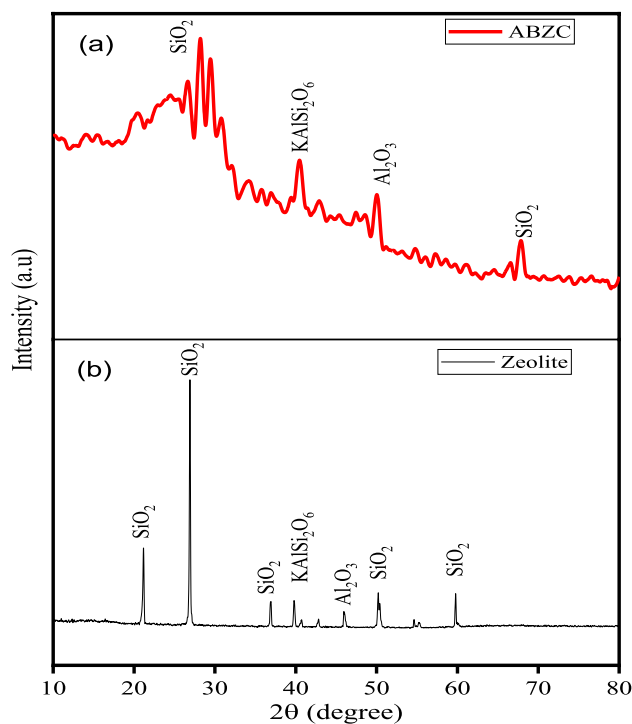


Fig. 8 XRD pattern of **a** ABZC nanocomposite and **b** zeolite catalyst

Table 3 Thermodynamic parameters after CR and MB removal performed between 293 and 313 K

Dye	Temp (K)	$\frac{1}{T}(\text{K}^{-1})$	K_L	$\ln K_L$	$\Delta G^\circ(\text{kJ/mol})$	$E_a(\text{kJ/mol})$	$\Delta H^\circ(\text{kJ/mol})$	$\Delta S^\circ(\text{kJ/mol/K})$
MB	293	0.0034	9.504	2.252	-5.485	19.65	17.21	77.70
	303	0.0033	12.68	2.540	-6.398	19.73		
	313	0.0032	15.97	2.771	-7.211	19.81		
	323	0.0031	18.19	2.901	-7.790	19.89		
CR	293	0.0034	1.925	0.6548	-1.595	11.82	9.379	37.55
	303	0.0033	2.259	0.8151	-2.053	11.90		
	313	0.0032	2.468	0.9032	-2.350	11.98		
	323	0.0031	2.779	1.022	-2.745	12.06		

of 21.4° , 27.01° , 36.8° , and 40° (JCPDS 083–2469) and alpha quartz (SiO_2) presented at 50.2° and 59.8° (JCPDS 078–1252). Also, KAlSi_2O_6 was represented at the characteristics peaks of 42.7° (JCPDS 26–0893). Finally, Al_2O_3 was indicated at peaks at 46.03° (JCPDS 075–0921).

3.5.2 Transmission electron microscopy and elemental compositions

The TEM micrographs and EDX compositions of elements at the prepared ABZC nanocomposite were assessed by TEM equipped with EDX. The TEM image investigated in Fig. 9a revealed rippled and entangled grey surface indicating the dominance of carbonaceous components in the composite material. The material surface indicated in Fig. 9b and c was covered by bright agglomerated particles that may be related to zeolite material. Moreover, these micrographs confirm the successful preparation of ABZC nanocomposite in nano-range with an average particle size of 30–40 nm. The EDX results (Fig. 9d) indicated that carbon was the most predominant in the composite matrix with 65.8% weight percent. There were sizable quantities of calcium, sodium, and silicon which confirm the presence of mesoporous zeolite [51]. The minor presence of other metal oxides originated from the biomass precursor. These results confirm the successful preparation of activated biochar/zeolite nanocomposite material that gives prediction about the material's ability to be evaluated as a good adsorbent toward adsorption of various dye types. Moreover, the presence of SiO_2 in the composite material postulates the good adsorption potential as an active silanol group in the activated carbon matrix that

possesses the strong potential to interact with both studied dye types for their decolorization [52].

3.5.3 BET surface area and pore sizes

The specific surface area analysis and surface morphological pore size distribution are vital parameters with a supreme influence on the uptake of MB and CR dyes. The porous structural properties establish the adsorbent surface's diffusion rate to material pores during physisorption [53]. The total pore volume, specific surface area, and average pore diameters of the prepared nanocomposites before and after activation are presented in Table 4.

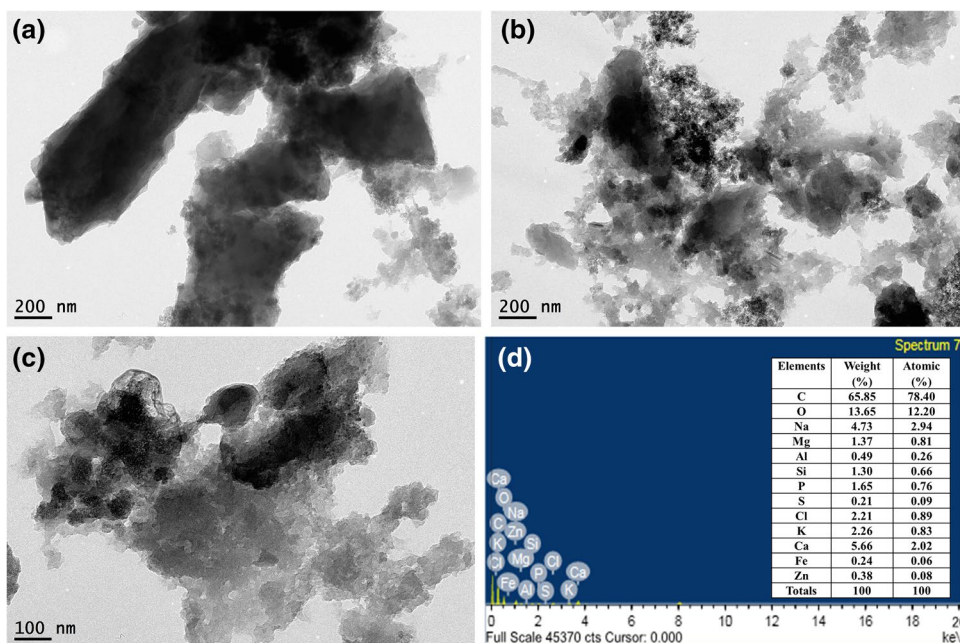
Nitrogen adsorption and desorption isotherm of composite material before and after activation reveal mesoporous solid with a type III isotherm conferring to IUPAC nomenclature, with varying pore diameter sizes as shown in Fig. 10.

It was evident from Table 4 that the alkaline activation reduced the particulate property of mean pore diameter from

Table 4 BET surface area results of the composite prior and after activation

Material	BET surface area (m^2/g)	Mean Pore diameter (nm)	Total pore volume (cm^3/g)
Composite before activation	1.85	19.84	0.0101
Composite after activation	15.3	3.865	0.0148

Fig. 9 TEM images (a, b, and c) and elemental composition (d) of the ABZC nanocomposite material



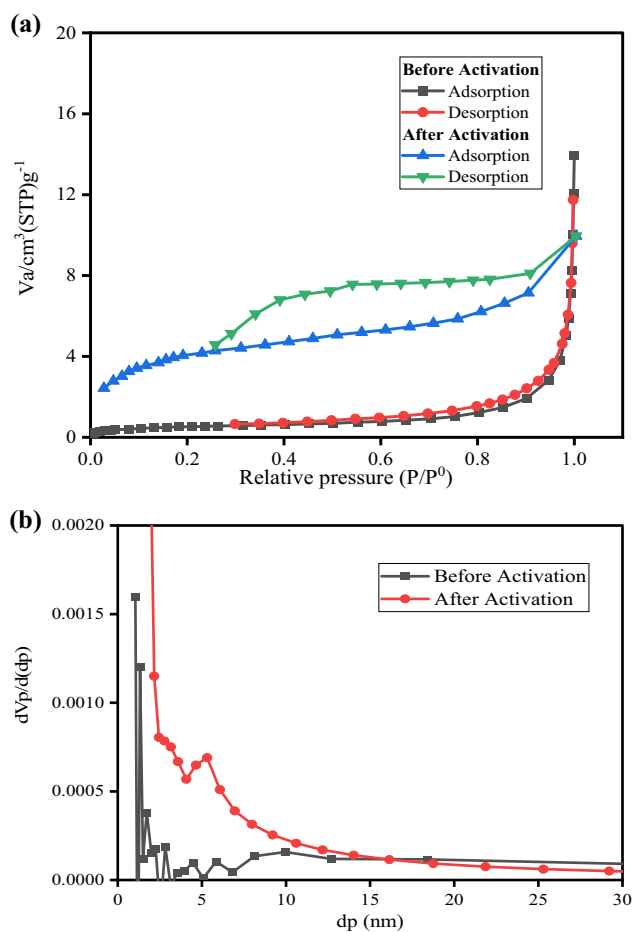


Fig. 10 N₂ adsorption–desorption isotherm and pore distribution before and after activation

19.84 to 3.865 nm but increased the total pore volume of the material from 0.0101 to 0.0148 cm³/g and specific surface area from 1.85 to 15.3 m²/g. These changes indicate that KOH reacts with ABZC nanocomposite to release volatile compounds initially uncarbonized in the fast pyrolysis process [54, 55]. Furthermore, the alkaline activation process

created additional pores due to reduction and oxidation reactions causing a decrease in pores from 19.84 to 3.865 nm [56]. The improvement in material pore volume is attributed to the rearrangement of the composite structure due to the increasing number of pores [57]

3.5.4 Scanning electron microscopy

The SEM micrograph images of the composite material after and before the removal of CR and MB dyes are investigated in Fig. 11. The SEM images revealed heterogeneous surfaces with dissimilar pore sizes and shapes. The material's morphology confirms the incorporation of the deposits of residual zeolite catalyst in the underlying char matrix, as revealed in Fig. 11a [58]. The chemical activation of the solid fraction introduced the pores as illustrated in the images. After adsorption process of both MB and CR dyes, a new thick layer coverage of material was deposited on the material surface, accompanied by the closure of existing pores causing smoothening of the micrograph. These results confirm the uptake of the dyes on the adsorbent material (Fig. 11b and c) [59].

3.5.5 FTIR analysis

FTIR molecular studies were performed in a wavelength region of 400–4000 cm⁻¹ to ascertain functional group variations of the adsorbent before and after the adsorption process (Fig. 12). The spectrum of the adsorbent revealed a broad peak at 3419 cm⁻¹ due to O–H vibrational stretching and a narrower at 1619 cm⁻¹ ascribing to C=C aromatic stretching, an intrinsic property of sp² graphitic carbon [52, 53]. In the fingerprint region, a peak that appeared at 1386 cm⁻¹ is attributed to S=O symmetrical stretching [60]. Other peaks appear at 1048 cm⁻¹ ascribing to Al–O–Si asymmetric vibration stretching and 870 cm⁻¹ accredited to Si–O–Si vibrations stretching [61]. The peak at 570 cm⁻¹ corresponds to the symmetrical stretching of the zeolite inner tetrahedra structure, which results in Si–O–Si deformation [62].

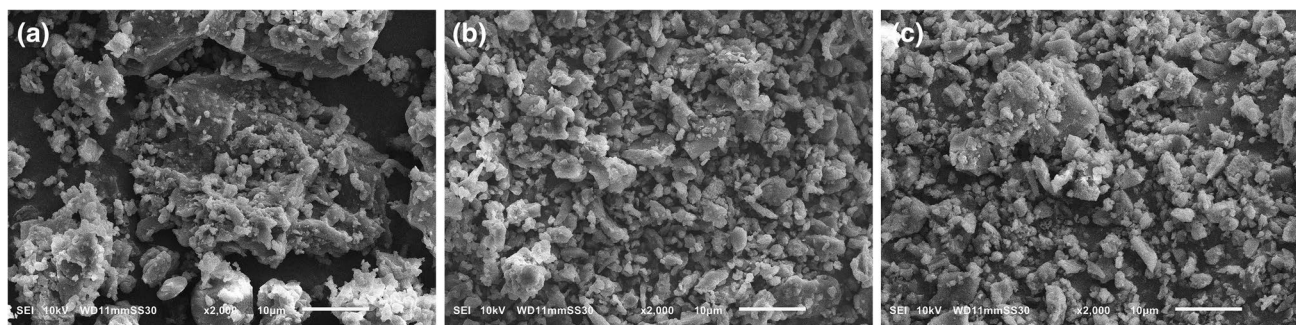


Fig. 11 SEM image of the composite material before and after dye adsorption, **a** free composite, **b** MB composite adsorbed, **c** CR composite adsorbed

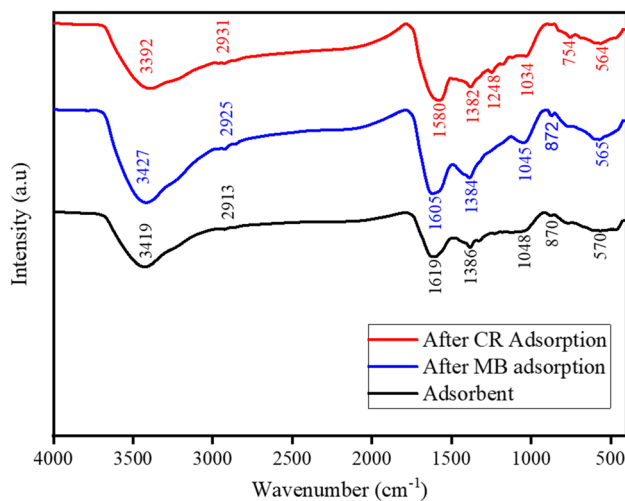


Fig. 12 FTIR spectra of the ABZC composite before and after dyes adsorption

The adsorption mechanism of CR and MB dyes can be described by alterations in the infrared spectra (IR) free dye composite and dye-bound composite. Quantifiable and sizeable changes in peaks were experienced for instance changes in peak intensities, shifts in peak positions, and disappearance of preexisting peaks. The peak at 3419 cm^{-1} for the free ABZC nanocomposite was shifted to 3427 cm^{-1} and 3392 cm^{-1} after MB and CR interactions, respectively, with weakened intensity. This is an indication that the dye molecule uptake by the synthesized nanocomposite material occurs by physical displacement of water postulating hydrogen bonding as the adsorption mechanism.

The peak presented at 1634 cm^{-1} of the aromatic ($\text{C}=\text{C}$) groups of ABZC nanocomposite was shifted to the lower wavelength of 1605 cm^{-1} for MB and 1580 cm^{-1} for CR dye adsorption with a reduction in intensity. The MB and CR dye molecules possess $\text{C}=\text{C}$ bonds with π electrons capable of interacting with π electrons of the nanomaterial via π - π electron stacking [63]. Other peaks at ABZC nanocomposite of 1048 cm^{-1} and 870 cm^{-1} were shifted to lower positions of 1045 cm^{-1} and 872 cm^{-1} for MB and 1034 cm^{-1} and 754 cm^{-1} for CR dye molecules. This indicated the interaction of the silanol group in the nanocomposite with the OH and SO_3^- of the MB and CR dye molecules via electrostatic interaction as revealed in Fig. S1. Moreover, the NH_2 group in the CR is potentially protonated to NH_4^+ . The situation initiates an interaction of polar moiety of NH_4^+ with $\text{Al}-\text{O}-\text{Al}$ causing a decrease in peak intensity [64]. The peak at 570 cm^{-1} shifted to the lower wavelength of 565 cm^{-1} for MB and 564 cm^{-1} for CR accompanied by a reduction of the spectrum intensity. The vibrating double four rings of zeolite structure consist of tetrahedra structure with $(\text{AlO}_4)^{5-}$ and $(\text{SiO}_4)^{4-}$ connected via oxygen atoms. The Si_4^+ possesses

the potential to be replaced by Al_3^+ via isomorphism to produce negative charges with further potential to bind with the cationic surface of MB and CR dyes [65, 66].

The deviations in the FTIR spectra of hydroxyl, aromatic, silicate, alumina, and deformed inner zeolite indicated an interlinkage between the functional group of the synthesized nanocomposite with a possible strong affinity towards adsorption of both MB and CR dyes [67].

3.6 Mechanistic postulation

A mechanism to elucidate the nature of adsorption can be proposed by an understanding of surface morphological changes, experimental conditions, and FTIR [68]. Accordingly, SEM micrographs demonstrated pore filling of the synthesized material by the dye as a possible mechanism. The FTIR spectrum of the synthesized free composite material and the dye-bound composite material indicated changes in positions and intensities of the major functional groups of ABZC nanocomposite. This implied Van der Waals forces, hydrogen bonding, π - π electron stacking, and electrostatic interaction as possible mechanisms [59]. Furthermore, the variations of pH as an experimental condition indicated the role of protonation and deprotonation to cause electrostatic interaction [58].

3.7 Validation of the performance of ABZC nanocomposite as adsorbent compared with various carbon-based materials

The uptake capacities of MB and CR dyes onto the composite material were compared with other available materials from the literature as indicated in Table 5. The results revealed that the composite material exhibited better uptake capacity than most carbon-based materials.

Table 5 Comparison of maximum adsorption capacity of the composite with other carbon-based adsorbents

Pollutant	Adsorbent	q_{max} (mg/g)	References
MB	Chitin Alp Kao nanocomposite	476.19	[60]
	Bamboo based activated carbon	454.20	[61]
	Graphene oxide	714	[62]
	Filtrisorb	476	[63]
	Green biochar/iron oxide composite	562	[64]
	ABZC	534.8	This study
CR	Chitin Alp Kao nanocomposite	104.6	[60]
	Ball milled bagasse	39.8	[65]
	Carbon nanotube	231.8	[66]
	Hierarchical nanotube	125	[67]
	Neem leaf powder	28.3–41.2	[68]
	ABZC	163.9	This study

4 Conclusions

This study highlighted a success in reusing activated biochar-zeolite nanocomposite for uptake of both dye types MB and CR. This novel nanocomposite was fabricated as a solid fraction from thermal catalytic conversion of biomass. The nano-diameter of prepared ABZC was determined using TEM imaging. Experimental dye adsorption parameters such as material dosage, temperature, and contact time positively influenced MB and CR dye removal process. Solution pH exhibited increased CR dye removal in the cationic medium, whereas MB dye removal was increased in the anionic medium. Thermodynamic parameters (ΔG° , ΔH° , ΔS°) were calculated. The negative ΔG° and positive ΔH° indicated the spontaneity and endothermic nature of the process, whereas the positive ΔS° indicated disorderliness at the solid–liquid interface. Equilibrium experimental data were best assessed by Freundlich, Langmuir, Temkin, and Dubinin–Radushkevich models. The equilibrium results best fitted the Langmuir model with R^2 of 0.9346 for MB and 0.9779 for CR dye. The maximum monolayer sorption capacities were calculated as 534.8 mg/g for MB and 163.9 mg/g for CR dye, indicating that the prepared material had competitive performance against other carbon-based adsorbents. The kinetics of the sorption process was pseudo-second-order and further hinted against intraarticular diffusion as the rate-determining step. FTIR studies postulated hydrogen bonding, Van der Waals forces, π - π electron stacking, and electrostatic interactions as possible adsorption mechanisms. This study is paramount to ensure the recovery of waste for beneficial usage.

Supplementary information The online version contains supplementary material available at <https://doi.org/10.1007/s13399-022-03299-y>.

Acknowledgements The first author is grateful to TICAD7, the corporation of Japanese and Egyptian government for providing support to pursue Msc studies. Great appreciation to Japan International Corporation Agency (JICA) for equipment and facilitations provided to accomplish this study.

Author contribution All authors contributed to the design of experiments. N.O. Rubangakene and H.S. Hassan performed the experimental work and the writing of the article. M.F. Elkady, A. Elwardany, analyzed the characterization data. M. Fujii, H. Sekiguchi, and M.F. Elkady reviewed and edited the manuscript.

Funding Open access funding provided by The Science, Technology & Innovation Funding Authority (STDF) in cooperation with The Egyptian Knowledge Bank (EKB).

Data availability The authors declare that all data supporting the findings of this research are available in this article.

Declarations

Ethical approval Not applicable.

Conflict of interest The authors declare no competing interests.

Open Access This article is licensed under a Creative Commons Attribution 4.0 International License, which permits use, sharing, adaptation, distribution and reproduction in any medium or format, as long as you give appropriate credit to the original author(s) and the source, provide a link to the Creative Commons licence, and indicate if changes were made. The images or other third party material in this article are included in the article's Creative Commons licence, unless indicated otherwise in a credit line to the material. If material is not included in the article's Creative Commons licence and your intended use is not permitted by statutory regulation or exceeds the permitted use, you will need to obtain permission directly from the copyright holder. To view a copy of this licence, visit <http://creativecommons.org/licenses/by/4.0/>.

References

- Mahmoodi NM, Saffar-Dastgerdi MH (2019) Zeolite nanoparticle as a superior adsorbent with high capacity: synthesis, surface modification and pollutant adsorption ability from wastewater. *Microchem J* 145:74–83. <https://doi.org/10.1016/j.microc.2018.10.018>
- Wang S, Ng CW, Wang W, Li Q, Hao Z (2012) Synergistic and competitive adsorption of organic dyes on multiwalled carbon nanotubes. *Chem Eng J* 197:34–40. <https://doi.org/10.1016/j.cej.2012.05.008>
- Elkady MF, Ibrahim AM, El-latif MMA (2011) Assessment of the adsorption kinetics, equilibrium and thermodynamic for the potential removal of reactive red dye using eggshell biocomposite beads. *DES* 278:412–423. <https://doi.org/10.1016/j.desal.2011.05.063>
- Piri F, Mollahosseini A, Khadir A, Milani Hosseini M (2019) Enhanced adsorption of dyes on microwave-assisted synthesized magnetic zeolite-hydroxyapatite nanocomposite. *J Environ Chem Eng* 7:103338. <https://doi.org/10.1016/j.jece.2019.103338>
- Koley P, Sakurai M, Takei T, Aono M (2016) Facile fabrication of silk protein sericin-mediated hierarchical hydroxyapatite-based bio-hybrid architectures: excellent adsorption of toxic heavy metals and hazardous dye from wastewater. *RSC Adv* 6:86607–86616. <https://doi.org/10.1039/c6ra12818a>
- Yang Y, Minh T, Nguyen P, Van HT, Trung Q (2022) Materials Science in Semiconductor Processing ZnO nanoparticles loaded rice husk biochar as an effective adsorbent for removing reactive red 24 from aqueous solution. *Mater Sci Semicond Process* 150:106960. <https://doi.org/10.1016/j.mssp.2022.106960>
- Hernández-Montoya V, Pérez-Cruz MA, Mendoza-Castillo DI, Moreno-Virgen MR, Bonilla-Petriciolet A (2013) Competitive adsorption of dyes and heavy metals on zeolitic structures. *J Environ Manage* 116:213–221. <https://doi.org/10.1016/j.jenvman.2012.12.010>
- Bharathi KS, Ramesh ST (2013) Removal of dyes using agricultural waste as low-cost adsorbents: a review. *Appl Water Sci* 3:773–790. <https://doi.org/10.1007/s13201-013-0117-y>
- Zaoui F, Zohra F, Liras M, Sebti H, Hachemaoui M, Mokhtar A, Beldjilali M, Bounaceur B, Boukoussa B (2021) Ultrasonic preparation of a new composite poly (GMA)@ Ru/TiO₂@Fe₃O₄: Application in the catalytic reduction of organic pollutants. *Mater Chem Phys* 260:124146. <https://doi.org/10.1016/j.matchemphys.2020.124146>

10. Khanday WA, Asif M, Hameed BH (2017) Cross-linked beads of activated oil palm ash zeolite/chitosan composite as a bio-adsorbent for the removal of methylene blue and acid blue 29 dyes. *Int J Biol Macromol* 95:895–902. <https://doi.org/10.1016/j.ijbiomac.2016.10.075>
11. Boughrara L, Zohra F, Sebti H, Choukchou-braham E, Bounaceur B, Ould S, Zaoui F (2021) Removal of Zn(II) and Ni(II) heavy metal ions by new alginate acid-ester derivatives materials. *Carbohydrates Polym* 272:118439. <https://doi.org/10.1016/j.carbpol.2021.118439>
12. Karaman C, Karaman O, Show P, Karimi-maleh H, Zare N (2022) Chemosphere Congo red dye removal from aqueous environment by cationic surfactant modified-biomass derived carbon : equilibrium, kinetic, and thermodynamic modeling, and forecasting via artificial neural network approach. *Chemosphere* 290:133346. <https://doi.org/10.1016/j.chemosphere.2021.133346>
13. Al-Ghouti MA, Li J, Salamh Y, Al-Laqtah N, Walker G, Ahmad MNM (2010) Adsorption mechanisms of removing heavy metals and dyes from aqueous solution using date pits solid adsorbent. *J Hazard Mater* 176:510–520. <https://doi.org/10.1016/j.jhazmat.2009.11.059>
14. Dawood S, Sen TK (2012) Removal of anionic dye Congo red from aqueous solution by raw pine and acid-treated pine cone powder as adsorbent : equilibrium, thermodynamic, kinetics, mechanism and process design. *Water Res* 46:1933–1946. <https://doi.org/10.1016/j.watres.2012.01.009>
15. Kumar KV, Kumaran A (2005) Removal of methylene blue by mango seed kernel powder. *Biochem Eng J* 27:83–93. <https://doi.org/10.1016/j.bej.2005.08.004>
16. Weng CH, Lin YT, Tzeng TW (2009) Removal of methylene blue from aqueous solution by adsorption onto pineapple leaf powder. *J Hazard Mater* 170:417–424. <https://doi.org/10.1016/j.jhazmat.2009.04.080>
17. Hamdaoui O, Chiha M (2007) Removal of methylene blue from aqueous solutions by wheat bran. *Acta Chim Slov* 54:407–418
18. Abdel-Khalek MA, Abdel Rahman MK, Francis AA (2017) Exploring the adsorption behavior of cationic and anionic dyes on industrial waste shells of egg. *J Environ Chem Eng* 5:319–327. <https://doi.org/10.1016/j.jece.2016.11.043>
19. Elkady M, Shokry H, Hamad H (2020) New activated carbon from mine coal for adsorption of dye in simulated water or multiple heavy metals in real wastewater. *Materials* 13:2498. <https://doi.org/10.3390/ma13112498>
20. Ren X, Cai H, Zhang Q, Zhang D, Lin X (2021) Evaluation of zeolite catalysts on product distribution during sweet sorghum bagasse catalytic pyrolysis. *Energy* 214. <https://doi.org/10.1016/j.energy.2020.118799>
21. Kamaraj M, Umamaheswari P (2017) Preparation and characterization of Groundnut shell activated carbon as an efficient adsorbent for the removal of Methylene blue dye from aqueous solution with microbiostatic activity. *J Mater Environ Sci* 8:2019–2025
22. Atugoda T, Gunawardane C, Ahmad M, Vithanage M (2021) Chemosphere Mechanistic interaction of ciprofloxacin on zeolite modified seaweed (*Sargassum crassifolium*) derived biochar : Kinetics, isotherm and thermodynamics. *Chemosphere* 281:130676. <https://doi.org/10.1016/j.chemosphere.2021.130676>
23. Saddeek Y, Shokry Hassan H, Abd Elfadeel G (2014) Fabrication and analysis of new bismuth borate glasses containing cement kiln dust. *J Non Cryst Solids* 403:47–52. <https://doi.org/10.1016/j.jnoncrysol.2014.07.004>
24. Jia L, Yu Y, peng Li Z, ning Qin S, rong Guo J, qiang Zhang Y, cheng Wang J, chun Zhang J, guo Fan B, jin Y (2021) Study on the Hg⁰ removal characteristics and synergistic mechanism of iron-based modified biochar doped with multiple metals. *Biore-sour Technol* 332:125086. <https://doi.org/10.1016/j.biortech.2021.125086>
25. B. Acemioğlu (2019) Removal of a reactive dye using NaOH-activated biochar prepared from peanut shell by pyrolysis process. *Int J Coal Prep Util* 0:1–23. <https://doi.org/10.1080/19392699.2019.1644326>
26. Mensah K, Mahmoud H, Fujii M, Shokry H (2022) Journal of Water Process Engineering Novel nano-ferromagnetic activated graphene adsorbent extracted from waste for dye decolonization. *J Water Process Eng* 45:102512. <https://doi.org/10.1016/j.jwpe.2021.102512>
27. Singh SR, Singh AP (2017) Adsorption of heavy metals from waste waters using waste biomass. *Int J Eng Res* V6:423–428. <https://doi.org/10.17577/ijertv6is010309>
28. Kolodyńska D, Hałas P, Franus M, Hubicki Z (2017) Zeolite properties improvement by chitosan modification—sorption studies. *J Ind Eng Chem* 52:187–196. <https://doi.org/10.1016/j.jiec.2017.03.043>
29. Diab KE, Salama E, Hassan HS, Abd El-moneim A, Elkady, (2021) Biocompatible MIP-202 Zr-MOF tunable sorbent for cost-effective decontamination of anionic and cationic pollutants from waste solutions. *Sci Rep* 11:1–13. <https://doi.org/10.1038/s41598-021-86140-2>
30. Ahmad R, Ansari K (2021) Comparative study for adsorption of congo red and methylene blue dye on chitosan modified hybrid nanocomposite. *Process Biochem* 108:90–102. <https://doi.org/10.1016/j.procbio.2021.05.013>
31. Rida K, Bouraoui S, Hadnine S (2013) Adsorption of methylene blue from aqueous solution by kaolin and zeolite. *Appl Clay Sci* 83–84:99–105. <https://doi.org/10.1016/j.clay.2013.08.015>
32. Islam MA, Ahmed MJ, Khanday WA, Asif M, Hameed BH (2017) Mesoporous activated coconut shell-derived hydrochar prepared via hydrothermal carbonization-NaOH activation for methylene blue adsorption. *J Environ Manage* 203:237–244. <https://doi.org/10.1016/j.jenvman.2017.07.029>
33. Han R, Zhang J, Han P, Wang Y, Zhao Z, Tang M (2009) Study of equilibrium, kinetic and thermodynamic parameters about methylene blue adsorption onto natural zeolite. *Chem Eng J* 145:496–504. <https://doi.org/10.1016/j.cej.2008.05.003>
34. Karadag D, Akgul E, Tok S, Erturk F, Kaya MA, Turan M (2007) Basic and reactive dye removal using natural and modified zeolites. *J Chem Eng Data* 52:2436–2441. <https://doi.org/10.1021/je7003726>
35. Dod R, Banerjee G, Saini S (2012) Adsorption of methylene blue using green pea peels (*Pisum sativum*): a cost-effective option for dye-based wastewater treatment. *Biotechnol. Bioprocess Eng* 17:862–874. <https://doi.org/10.1007/s12257-011-0614-5>
36. Hartman RL, Fogler HS (2005) Reaction kinetics and mechanisms of zeolite dissolution in hydrochloric acid. *Ind Eng Chem Res* 44:7738–7745. <https://doi.org/10.1021/ie0504349>
37. Batool A, Valiyaveetil S (2021) Chemical transformation of soya waste into stable adsorbent for enhanced removal of methylene blue and neutral red from water. *J Environ Chem Eng* 9:104902. <https://doi.org/10.1016/j.jece.2020.104902>
38. Elkady MF, Hassan HS, Amer WA, Salama E, Algarni H, Shaaban ER (2017) Novel magnetic zinc oxide nanotubes for phenol adsorption: mechanism modeling. *Materials* 10:1355. <https://doi.org/10.3390/ma10121355>
39. Shokry Hassan H, Kashyout AB, Morsi I, Nasser AAA, Raafat A (2014) Fabrication and characterization of gas sensor micro-arrays. *Sens Biosensing Res* 1:34–40. <https://doi.org/10.1016/j.sbsr.2014.04.001>
40. Singh S, Sidhu GK, Singh H (2019) Removal of methylene blue dye using activated carbon prepared from biowaste precursor, Indian. *Chem Eng* 61:28–39. <https://doi.org/10.1080/00194506.2017.1408431>
41. Guo JZ, Li B, Liu L, Lv K (2014) Removal of methylene blue from aqueous solutions by chemically modified bamboo. *Chemosphere* 111:225–231. <https://doi.org/10.1016/j.chemosphere.2014.03.118>

42. Al-dahri T, AbdulRazak AA, Rohani S (2020) Preparation and characterization of Linde-type A zeolite (LTA) from coal fly ash by microwave-assisted synthesis method: its application as adsorbent for removal of anionic dyes. *Int J Coal Prep Util* 00:1–14. <https://doi.org/10.1080/19392699.2020.1792456>
43. Fernandes AN, Almeida CAP, Debacher NA, Sierra MMDS (2010) Isotherm and thermodynamic data of adsorption of methylene blue from aqueous solution onto peat. *J Mol Struct* 982:62–65. <https://doi.org/10.1016/j.molstruc.2010.08.006>
44. Sharma P, Borah DJ, Das P, Das MR (2016) Cationic and anionic dye removal from aqueous solution using montmorillonite clay: evaluation of adsorption parameters and mechanism. *Desalin Water Treat* 57:8372–8388. <https://doi.org/10.1080/19443994.2015.1021844>
45. Hema M, Arivoli S (2009) Rhodamine B adsorption by activated carbon: kinetic and equilibrium studies, *Indian. J Chem Technol* 16:38–45
46. Fungaro DA, Grosche LC, Pinheiro AS, Izidoro JC (2010) Adsorption of methylene blue from aqueous solution on zeolitic material and the improvement as toxicity removal to living organisms, 2
47. Yusuff AS, Olateju II (2018) Experimental investigation of adsorption capacity of anthill in the removal of heavy metals from aqueous solutions. *Environ Qual Manag* 27:53–59. <https://doi.org/10.1002/tqem.21536>
48. Zhang L, Yao Z, Zhao L, Li Z, Yi W, Kang K, Jia J (2021) Synthesis and characterization of different activated biochar catalysts for removal of biomass pyrolysis tar. *Energy* 232:120927. <https://doi.org/10.1016/j.energy.2021.120927>
49. Shokry H, Elkady M, Hamad H (2019) Nano activated carbon from industrial mine coal as adsorbents for removal of dye from simulated textile wastewater: Operational parameters and mechanism study. *J Mater Res Technol* 8:4477–4488. <https://doi.org/10.1016/j.jmrt.2019.07.061>
50. Elkady M, Shokry H, Hamad H (2020) New activated carbon from mine coal for adsorption of dye in simulated water or multiple heavy metals in real wastewater, *Materials (Basel)*. 13
51. Litefti K, Freire MS, Stitou M, González-Álvarez J (2019) Adsorption of an anionic dye (Congo red) from aqueous solutions by pine bark. *Sci Rep* 9:1–11. <https://doi.org/10.1038/s41598-019-53046-z>
52. Elkady MF, Shokry Hassan H, El-Sayed EM (2011) Basic violet decolorization using alginate immobilized nanozirconium tungstovanadate matrix as cation exchanger. *J Chem* 2015:385741. <https://doi.org/10.1155/2015/385741>
53. Barnaby AG, Reid R, Rattray V, Williams R, Denny M (2016) Characterization of Jamaican *Delonix regia* and *Cassia fistula* Seed Extracts. *Biochem Res Int* 2016:3850102. <https://doi.org/10.1155/2016/3850102>
54. Milato JV, França RJ, Marques MRC (2021) Pyrolysis of oil sludge from the offshore petroleum industry: influence of different mesoporous zeolites catalysts to obtain paraffinic products. *Environ Technol (United Kingdom)* 42:1013–1022. <https://doi.org/10.1080/09593330.2019.1650833>
55. Milato JV, França RJ, Marques Calderari MRC (2020) Co-pyrolysis of oil sludge with polyolefins: evaluation of different zeolites to obtain paraffinic products, *J Environ Chem Eng* 8. <https://doi.org/10.1016/j.jece.2020.103805>
56. Zamani F, Rezapour M, Kianpour S (2013) Immobilization of L-Lysine on zeolite 4A as an organic-inorganic composite basic catalyst for synthesis of α , β -unsaturated carbonyl compounds under mild conditions. *Bull Korean Chem Soc* 34:2367–2374. <https://doi.org/10.5012/bkcs.2013.34.8.2367>
57. Prajaputra V, Abidin Z, Widiatmaka, Suryaningtyas DT, Rizal H (2019) Characterization of Na-P1 zeolite synthesized from pumice as low-cost materials and its ability for methylene blue adsorption. *IOP Conf Ser Earth Environ Sci* 399. <https://doi.org/10.1088/1755-1315/399/1/012014>
58. Boughrara L, Zaoui F, Guezoul M, Zohra F (2022) New alginate acid derivatives ester for methylene blue dye adsorption: kinetic, isotherm, thermodynamic, and mechanism study. *Int J Biol Macromol* 205:651–663. <https://doi.org/10.1016/j.ijbiomac.2022.02.087>
59. Yang G, Wu L, Xian Q, Shen F, Wu J, Zhang Y (2016) Removal of Congo red and methylene blue from aqueous solutions by vermicompost-derived biochars. 1–18. <https://doi.org/10.1371/journal.pone.0154562>
60. Cao YL, Pan ZH, Shi QX, Yu JY (2018) Modification of chitin with high adsorption capacity for methylene blue removal. *Int J Biol Macromol* 114:392–399. <https://doi.org/10.1016/j.ijbiomac.2018.03.138>
61. Hameed BH, Din ATM, Ahmad AL (2007) Adsorption of methylene blue onto bamboo-based activated carbon: kinetics and equilibrium studies. *J Hazard Mater* 141:819–825. <https://doi.org/10.1016/j.jhazmat.2006.07.049>
62. Yang ST, Chen S, Chang Y, Cao A, Liu Y, Wang H (2011) Removal of methylene blue from aqueous solution by graphene oxide. *J Colloid Interface Sci* 359:24–29. <https://doi.org/10.1016/j.jcis.2011.02.064>
63. Elkady MF, Shokry Hassan H (2015) Invention of hollow zirconium tungstovanadate at nanotube morphological structure for radionuclides and heavy metal pollutants decontamination from aqueous solutions. *Nanoscale Res Lett* 10:1–6. <https://doi.org/10.1186/s11671-015-1180-0>
64. Zhang P, O'Connor D, Wang Y, Jiang L, Xia T, Wang L, Tsang DCW, Ok YS, Hou D (2020) A green biochar/iron oxide composite for methylene blue removal. *J Hazard Mater* 384:121286. <https://doi.org/10.1016/j.jhazmat.2019.121286>
65. Zhang Z, Moghaddam L, O'Hara IM, Doherty WOS (2011) Congo Red adsorption by ball-milled sugarcane bagasse. *Chem Eng J* 178:122–128. <https://doi.org/10.1016/j.cej.2011.10.024>
66. Zare K, Sadegh H, Shahryari-Ghoshekandi R, Maazinejad B, Ali V, Tyagi I, Agarwal S, Gupta VK (2015) Enhanced removal of toxic Congo red dye using multi walled carbon nanotubes: kinetic, equilibrium studies and its comparison with other adsorbents. *J Mol Liq* 212:266–271. <https://doi.org/10.1016/j.molliq.2015.09.027>
67. Yu M, Zhao S, Wu H, Asuha S (2013) Efficient removal of Congo red by magnetically separable mesoporous TiO₂ modified with γ -Fe₂O₃. *J Porous Mater* 20:1353–1360. <https://doi.org/10.1007/s10934-013-9721-3>
68. Elkady MF, Shokry Hassan H, Salama E (2016) Sorption profile of phosphorus ions onto ZnO nanorods synthesized via sonic technique *J Eng* 2016:2308560. <https://doi.org/10.1155/2016/2308560>

Publisher's note Springer Nature remains neutral with regard to jurisdictional claims in published maps and institutional affiliations.